Stochastic geometrical modeling of solid oxide cells electrodes validated on 3D reconstructions

Hamza Moussaoui, Jérôme Laurencin, Yann Gavet, Gérard Delette, Maxime Hubert, Peter Cloetens, Tristan Le Bihan, Johan Debayle

Stochastic Geometrical Modeling of Solid Oxide Cells Electrodes Validated on 3D Reconstructions

H. Moussaoui[1,2,*], J. Laurencin[1], Y. Gavet[2], G. Delette[1], M. Hubert[1,3], P. Cloetens[3], T. Le Bihan[4], J. Debayle[2]

[1] Univ. Grenoble Alpes – CEA/LITEN, 38054, Grenoble, France
[2] Ecole Nationale Supérieure des Mines de Saint-Etienne, SPIN, CNRS 5307, LGF, F-42023 Saint-Etienne, France
[3] European Synchrotron Radiation Facility (ESRF), 38000, Grenoble, France
[4] CEA, DAM, Le Ripault, F-37260, Monts, France

Abstract. An original 3D stochastic model, based on the truncated plurigaussian random fields, has been adapted to simulate the complex microstructure of SOC electrodes. The representativeness of the virtual microstructures has been checked on several synchrotron X-ray and FIB-SEM tomographic reconstructions obtained on typical LSCF, LSC and Ni-YSZ electrodes. The validation step has been carried out by comparing numbers of electrode morphological properties as well as the phase effective diffusivities. This analysis has shown that the synthetic media mimic accurately the complex microstructure of typical SOC electrodes. The model capability to simulate different types of promising electrode architectures has also been investigated. It has been shown that the model is able to generate virtual electrode prepared by infiltration resulting in a uniform and continuous thin layer covering a scaffold. With a local thresholding depending on the position, continuous graded electrodes can be also produced. Finally, the model offers the possibility to introduce different correlation lengths for each phase in order to control the local topology of the interfaces. All these cases illustrate the model flexibility to generate various SOC microstructures. This validated and flexible model can be used for further numerical microstructural optimizations to improve the SOC performances.

Keyword: Solid Oxide Cell, 3D microstructure model, truncated plurigaussian random fields, X-ray tomography, Electrode design.
*Corresponding author: Telephone: +33 (0)438784360, Fax: +33 (0)438784139,
E-mail: hamza.moussaoui@cea.fr

1. Introduction

The climate change, the rarefaction of fossil fuels in conjunction with the growing worldwide demand for energy have drastically increased the need of clean and sustainable energy sources. However, the use of intermittent renewable technologies such as solar panels or wind turbines requires new solutions to match the fluctuations between the demand and the production. A new flexible energetic vector for storing energy is thus required to absorb the peaks of electricity production or consumption. The dihydrogen gas, which presents a high ratio of energy to mass, is considered as one of the most relevant choices for this vector. In this view, the high-temperature electrochemical systems appear as a promising technology for the efficient and reversible gas to electricity conversion [1,2]. Indeed, thanks to their high flexibility, the same electrochemical device can be alternatively used in fuel cell mode for electrical power generation and steam electrolysis mode for dihydrogen production [3] (i.e. in Solid Oxide Fuel Cell – SOFC – mode or in Solid Oxide Electrolysis Cell – SOEC – mode). This type of high-temperature electrolyser-fuel-cell is constituted by a stack of elementary Solid Oxide Cells (SOCs), each one being composed of a dense electrolyte sandwiched between two porous electrodes. State-of-the-art for SOC components are Yttria Stabilized Zirconia (YSZ) for the electrolyte and Ni-YSZ cermet for the H_2 electrode [1,2]. The O_2 electrode is currently made of Mixed Ionic Electronic Conductors (MIECs) such as Lanthanum Strontium Cobalt (LSC) or Lanthanum Strontium Cobalt Ferrite (LSCF).

The manufacturing routes for Solid Oxide Cells (SOCs) are based on typical ceramic processing such as screen printing, tape casting or dip-coating [4]. Other original methods, based on catalyst infiltration [5] or Electrostatic Spray Deposition (ESD) [6], have been recently proposed to improve the SOCs efficiency. Thanks to the large variety of these methods, a wide range of electrode microstructures is liable to be produced and adapted to each SOC applications (*i.e.* fuel cell, steam electrolysis, reversible system, etc.). Indeed, the microstructure of the electrodes plays a major role in the global cell performances by controlling the rates of the electrochemical reactions which depend on each SOC application [7-10]. As a consequence, the electrode microstructure can be tuned to design more efficient SOC for each particular utilization. Nevertheless, the electrodes present a complex three dimensional microstructure for which the basic relationships between the three-dimensional characteristics of the microstructure and the electrode properties are not still precisely understood. Thus,

several studies [11-14] have been recently proposed in an attempt to improve the knowledge of such relations, which are essential before optimizing the microstructure.

During the last decades, advances in 3D characterization have been achieved to image the SOC electrode microstructure. Different techniques based on Focused Ion Beam sectioning coupled with a Scanning Electron Microscope (FIB-SEM) [15-17], X-ray absorption tomography [18-20] or holotomography [10,21-22] have been successfully employed to reconstruct the SOCs electrodes microstructures with a high spatial resolution (at the scale of few tens of nanometers). Some authors [14,17,23-26] have taken advantage of these techniques to study the links between the electrode microstructural parameters. However, this approach is time consuming as it needs the manufacturing and the characterization of several cells. For this reason, the number of reconstructed electrodes was limited. In general, the evolution of microstructural parameters such as the specific surface area, the tortuosity factor or the Triple Phase Boundaries lengths TPBls (defined as the lines where the electronic, ionic and gas phase meet) are plotted as function of the phase volume fractions with few points [23,24]. These data are thus insufficient to fully understand and validate the proposed complex relationships linking the electrode microstructure parameters [11,13]. In order to increase the amount of data required to fit accurately these relationships, an alternative method consists of generating representative synthetic microstructures by numerical means.

For this purpose, a lot of attempts have been devoted to the development of relevant 3D geometrical models able to mimic the actual microstructure of both two-phase electrodes (i.e. porous LSCF for example) and three-phase composite electrodes (i.e. Ni-YSZ cermet for example). Most of the published methods are related to stochastic models based on random sphere packing algorithms [27,28]. In this frame, many authors have assumed a uniform particle size whereas only few studies have taken into account a more realistic distribution on the sphere radii [29-30]. As a general matter, the sphere packing algorithms are decomposed into 2 steps. The first one is related to the creation of "seeds" corresponding to the positioning of the spheres. The second step is dedicated to the simulation of the "sintering" process in order to densify the microstructure up to the desired porosity. The first step can be done by the so-called "drop & roll" algorithm [9,29,31,32] or by the random positioning of "seeds" on a lattice structure [27,33,34]. However, these methods are too much constrained, and hence, they are not able to account for the full stochastic nature of the actual SOCs electrodes. For example, the positioning of spheres on a lattice results in a structuration of the final microstructure that is not realistic

regarding the SOC microstructure. Furthermore, the Drop and Roll method yields an irrelevant anisotropy in the synthetic microstructures [37]. To overcome this issue, some authors have developed algorithms with a pure random positioning of spheres [35,36]. The second step of the sphere packing methods is based on basic geometrical operations to increase the surface contact between particles (i.e. sphere radius expansion [32,33,35,37] or overlapping [9,29,31] and creation of necks [34]). Aside from these pure geometrical approaches, the Discrete Element Method (DEM) has also been employed to simulate the initial sphere packing by computing the mechanical contact between the particles [12,38]; while the densification can be simulated by modelling the physical sintering process [12]. All these iterative methods need rather intensive CPU resources especially for the DEM computations.

In addition to the sphere packing, other stochastic models based on geostatistical simulations can be used to generate synthetic microstructures [39]. Different iterative methods based on the minimization of correlation functions between the synthetic microstructure and a real segmented image have been used to generate three-phase Ni-YSZ electrodes [40,41]. It is worth mentioning that non-iterative methods can be useful to simulate a microstructure in a short time. For this purpose, Neumann et al. [42] have proposed a generalization of a multi-steps model decomposed in a homogeneous Poisson point process, a beta skeleton algorithm followed by the voxel phase labelling. With the same objective, Lanzini et al. [43] have applied the truncated Gaussian random field model to the SOC electrodes by considering a medium constituted of two phases (i.e. the pores with one solid phase). Abdallah et al. [44] have applied the Boolean random sets and the truncated plurigaussian random field model to generate a porous Ni-YSZ composite electrode. In the last case, the three sets related to the three electrode phases were obtained with set operations on the two underlying segmented independent Gaussian random fields.

It is worth noting that few studies have been devoted to validate the morphological representativeness of the numerical SOC microstructures compared to the real ones. As a general matter, the sphere packing methods yield a final microstructure that keeps the geometry of the initial spheres. Therefore, as pointed out in [28], the relevance of this morphology can be questionable if compared to the real SOC electrode microstructure in which the phases exhibit a complex and continuous shape. Nevertheless, as discussed in Neumann et al. [42], these approaches allow qualitative conclusions for the microstructural relationships even if ‘their applicability to real materials are still unclear’. For instance, Nishida et al. [27] have succeeded with a random sphere packing model to reproduce the experimental dependence of TPBs

density with the solid phase volume faction. However, Choi et al. [45] have compared a FIB-SEM reconstruction to a numerical microstructure generated by sphere packing. They obtained significant differences in the resulting structures.

For the other approaches based on geostatistical simulations, Neumann et al. [42] have validated their model on a 3D reconstruction of a real Ni-YSZ electrodes. The virtual microstructure fitted on the reconstruction presents a good agreement not only visually but also quantitatively in terms of morphological parameters (geometrical tortuosity factors, constrictivities, density of TPBs after smoothing) and phase effective conductivities. Nevertheless, they found a significant mismatch for the interfacial specific surface area. Abdallah et al. [44] have fitted their 3D synthetic microstructures on the covariance function measured on 2D SEM micrographs of a Ni-YSZ cermet. They have shown that the Boolean sets is not a relevant method for SOC electrode modelling. However, the microstructure generated with the plurigaussian model was found 'to be visually very close to the materials'. Moreover, in addition to the fitted covariance functions, they also found a good agreement in terms of phase size distributions and the linear erosion functions (measured on the 2D SEM images).

In the present study, the truncated plurigaussian random field model has been employed to generate synthetic microstructures of SOC electrodes. A specific attention has been paid to fully validate the method on several X-ray holotomography and FIB-SEM 3D reconstructions obtained for both O_2 and H_2 electrodes. The model validation step has been carried through a set of morphological parameters and by computing phase effective diffusivities. It is worth noting that the present model includes a generalization, which was initially proposed in Galli et al. [46] and detailed in Armstrong et al. [47], for the combination and thresholding of independent random fields. This method was adapted here to the SOCs electrodes in order to improve the relevance and the representativeness of the synthetic microstructure. The method also offers the possibility to have a more flexible numerical tool. Two correlation lengths have been thus introduced for the electrode solid phases. The capacity of the approach to mimic different kind of electrode microstructures and architectures is illustrated and discussed on several examples.

2. Random Field Model description for SOC electrodes

2.1 Two-phase materials for O_2 electrode

The truncated Gaussian random field model has been used to generate 3D microstructures of typical O_2 electrodes made of porous LSCF or LSC. For a two-phase material, a general description of the method can be found in [39,48,49]. Only the main steps of the procedure are thus reminded hereafter by underlying the specificities that were adopted to model the SOC electrode microstructures.

Main model assumptions – A statistically stationary, isotropic and homogeneous porous microstructure has been considered in the model. Such assumption is well verified on 'typical' commercial SOCs electrodes obtained by screen printing or tape casting [21,50]. Moreover, it is generally considered that the covariance function contains the most relevant morphological information required to reconstruct a microstructure [51]. As a consequence, it has been assumed that the microstructure of a two-phase electrode (X and $\overline{X}$, where X refers to one phase and $\overline{X}$ the other) can be characterized through the covariance function $C_X(h)$ which is used as the only input data for the simulations. From a mathematical point of view, $C_X(h)$ is expressed as the probability that two points separated by a distance h belong to the same phase X:

$$C_X(h) = P(z \in X, z+h \in X) \quad \text{for } z \in \Omega \tag{1}$$

Where Ω denotes the 3D domain. The covariance function provides information on the phase volume fraction ε_X:

$$0 \le C_X(h) \le \varepsilon_X = C_X(0) \tag{2}$$

It is also linked to the phase specific surface area S_p^X, which is simply defined as the total surface area of the interface between this phase X and its complementary $\overline{X}$ normalized by the domain volume V_Ω [51]:

$$S_p^X = -\frac{4}{V_\Omega}\left.\frac{dC_X}{dh}\right|_{h=0} \tag{3}$$

In a general point of view, the covariance function describes how the phase is distributed in the 3D space. It tends to an asymptotic value corresponding to the square of the volume fraction:

$\lim_{h\to+\infty} C_X(h) = \varepsilon_X^2$. The distance to reach this asymptotic bound is defined as the range of the covariance and can be ascribed to the phase characteristic length [51].

Description of the model steps – Basically, the model consists in the generation of a stationary and normal centered random Gaussian field $G_X(z)$ that exhibits the same spatial correlation than the real homogenous microstructure (described with the covariance function). The two phases, *X* and $\overline{X}$, of the synthetic microstructure are thus obtained by thresholding $G_X(z)$:

$$X = \{z; G_X(z) \geq \lambda_X\} \tag{4}$$

Where λ_X denotes the threshold.

(*i*) In order to determine λ_X, it is reminded that $G_X(z)$ follows the law of a standard normal distribution (of mean value μ=0 and variance σ^2=1): $G_X(z) \sim N(0,1)$. Therefore, the threshold can be related to the phase volume fraction with the following relation:

$$\varepsilon_X = P\{G_X(z) \geq \lambda_X\} = \int_{\lambda_X}^{\infty} p(x)dx \tag{5}$$

Where *p(x)* is the continuous probability density function of the normal distribution $N(0,1)$. The threshold can be easily deduced from (5) as illustrated in Fig. 1:

$$\varepsilon_X = 1 - \int_{-\infty}^{\lambda_X} \frac{1}{\sqrt{2\pi}} \exp\left(-\frac{1}{2}x^2\right)dx \tag{6}$$

(*ii*) As described for the first time by Alder et al. [52] and further developed by Liang et al. [53], the field $G_X(z)$ can be generated by the convolution of an uncorrelated Gaussian random noise *U(z)* with a normalized and symmetric weight function *ω(h)*:

$$\begin{gathered} G_X(z) = U(z) * \omega(h) = \int_{h\in\Omega} U(z-h)\omega(h)dh \\ \text{with}: \quad \sum_{\Omega} \omega^2(h) = 1 \quad \text{and} \quad \omega(h) = \omega(-h) \quad \forall h \end{gathered} \tag{7}$$

This operation can be interpreted as the filtering of the uncorrelated random noise *U(z)* with the weight function *ω(h)*. The objective of this operation is to introduce the requested spatial correlation in $G_X(z)$. Therefore, *ω(h)* is linked to the correlation function $\rho_X(h)$ of the Gaussian random field defined as follows:

$$\rho_X(h) = \mathrm{cov}\{G_X(z), G_X(z+h)\} \tag{8}$$

(*iii*) To determine the weight function, it can be shown that the auto-convolution of $\omega(h)$ is equal to $\rho_X(h)$ (cf. appendix):

$$(\omega * \omega)(h) = \rho_X(h) \tag{9}$$

(*iv*) The correlation function $\rho_X(h)$ of the random field is associated to the covariance function of the real microstructure $C_X(h)$ through the following relation (cf. demonstration in appendix):

$$C_X(h) - \varepsilon_X = \frac{1}{2\pi} \int_1^{\rho_X(h)} \frac{1}{\sqrt{1-r^2}} \exp\left\{\frac{-\lambda_X^2}{1+r}\right\} dr \tag{10}$$

To summarize, the method is decomposed into a sequence of successive steps consisting of:

(1) The determination of the threshold λ_X with the phase volume fraction (eq. (6)),

(2) The computation of the correlation function $\rho_X(h)$ with the covariance $C_X(h)$ of the real microstructure (eq. 10),

(3) The generation of the random field $G_X(z)$ by combining eqs. (7) and (9),

(4) The segmentation of $G_X(z)$ with the threshold λ_X to obtain the final synthetic microstructure.

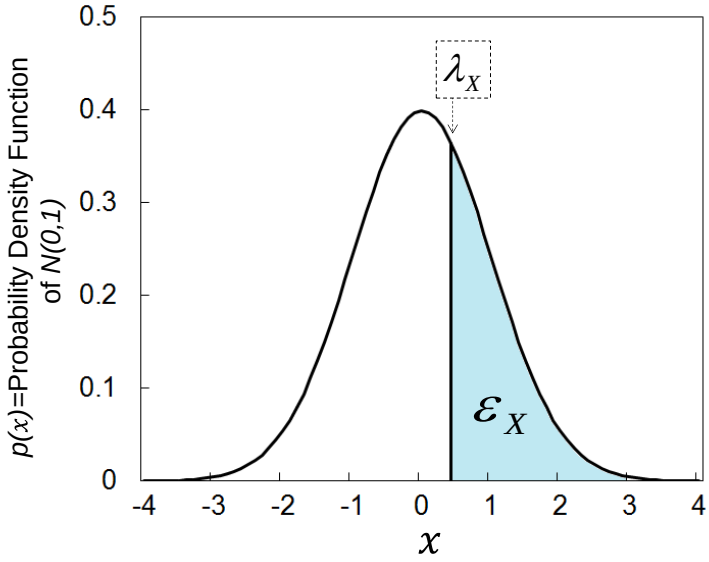

Fig. 1. Distribution and definition of the threshold for a two-phase electrode: the Gaussian field is proportion to a normal distribution segmented with a constant threshold.

Numerical implementations – The model steps have been implemented in Matlab® software. Instead of directly calculating computationally expensive convolutions, the use of Fast Fourier Transform (FFT) must allow to drastically reduce the time for generating the microstructure. For this purpose, the convolution products (7) and (9) have been carried out in the Fourier space by using FFT transforms:

$$G_X(z) = FFT^{-1}\left\{FFT\left(U(z)\right) \times \sqrt{FFT\left(\rho(h)\right)}\right\} \tag{11}$$

Thanks of the symmetry of $U(z)$ and $\rho(h)$, it is worth mentioning that their FFT transforms in eq. (11) lead to positive and real numbers (the imaginary part is nil). Moreover, it has been shown by Lang et al. [54] that the error induced by the FFT approximation is negligible for a sufficiently fine discretization of the domain. Thanks to this model implementation, the simulations are very fast and allow the generation of virtual microstructures in a very short time compared to other iterative methods. For example, considering a volume of 9x9x9 µm^3 with a voxel size of 25 nm, the virtual microstructure of the studied two-phase electrode (for Cell-A: cf. Section 4.1) is created in ~8 seconds by using only one CPU (Intel© Xenon©). In the objective to quantitatively compare the iterative and non-iterative methods, the same microstructure has been generated by using an in-house overlapping sphere packing algorithm [81]. With the same computational resources, a time of ~90 minutes is needed to obtain the synthetic microstructure. This result highlights the low computational expense requested by the random field methods in comparison to other iterative techniques. It can be noticed in both cases, the memory usage is about 756 Megabytes. Moreover, the time and the memory linearly increase with the number of voxels.

It can be noticed that a least square method is used to solve eq. (10) and to compute the discrete correlation function $\rho_X(h)$ by minimization on $C_X(h)$. However, it has been found that the direct use of the numerical expression of $\rho_X(h)$ to generate the microstructure yields an irrelevant noise at the interface between the phases (Fig. 2). To overcome this issue, Abdallah et al. [44] have applied a low pass Gaussian filter on the random field $G_X(z)$ to remove the small-length artifacts. Alternatively, an analytical model for the correlation function [39,48,55] can be fitted on the discrete values of $\rho_X(h)$ and used in the procedure. Different noise-free models and their combinations [39,48] have been tested. It has been found that the exponential

correlation of second order (Gaussian) is the most suitable function to obtain a good fit of $\rho_X(h)$:

$$\rho(h) = \exp\left\{\frac{-h^2}{2\ell^2}\right\} \tag{12}$$

Where ℓ is the fitted correlation length. As illustrated in Fig. 2, the resulting microstructure does not present noise at the phase interface.

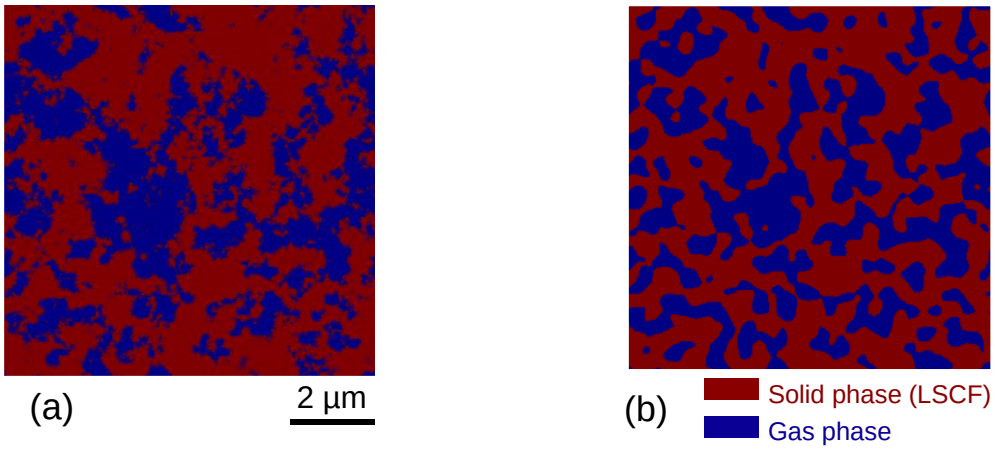

Fig. 2. 2D slice extracted from the 3D virtual microstructure for the LSCF electrode of Cell-A (cf. Section 3.1). (a) Image obtained with the discrete correlation function $\rho_X(h)$ after minimization on $C_X(h)$ (without fitting). (b) Image obtained by fitting the Gaussian exponential function on the discrete values of $\rho_X(h)$ after minimization on $C_X(h)$.

The virtual microstructure for the two-phase electrode can be built either by generating the solid or the gas phase. In practice, no significant differences have been found for the typical tested electrodes. Besides, taking into account the stochastic nature of the method, different realizations result in different microstructures. Nevertheless, it has been found that the microstructures exhibit the same characteristics if considering a volume large enough to be statistically representative.

2.2 Three-phase materials for H_2 electrode

Description of the model steps – In the present article, a method [46,47] allowing the combination and thresholding of two independent Gaussian random fields has been used to simulate typical three-phase SOC electrode microstructures. The method is based on the

generation of two fields $G_X(z)$ and $G_Y(z)$ with the covariance functions $C_X(h)$ and $C_Y(h)$ related to the phases X and Y of the real microstructure (i.e. for instance *X*=Ni, *Y*=YSZ and porosity= $\overline{X \cup Y}$).

The process to compute $G_X(z)$ or $G_Y(z)$ is the same than the one depicted in the previous section. The two fields are then combined to form a bigaussian random field $G_{XY} = \{G_X(z); G_Y(z)\}$ that follows a standard normal bivariate distribution $G_{XY}(z) \sim N\left(\mu = \begin{bmatrix} 0 \\ 0 \end{bmatrix}, \Sigma = \begin{bmatrix} 1 & 0 \\ 0 & 1 \end{bmatrix}\right)$ whose the probability density function *p(x,y)* is (Fig. 3a):

$$p(x,y) = \frac{1}{2\pi} \exp\left\{\frac{-\left(x^2 + y^2\right)}{2}\right\} \tag{13}$$

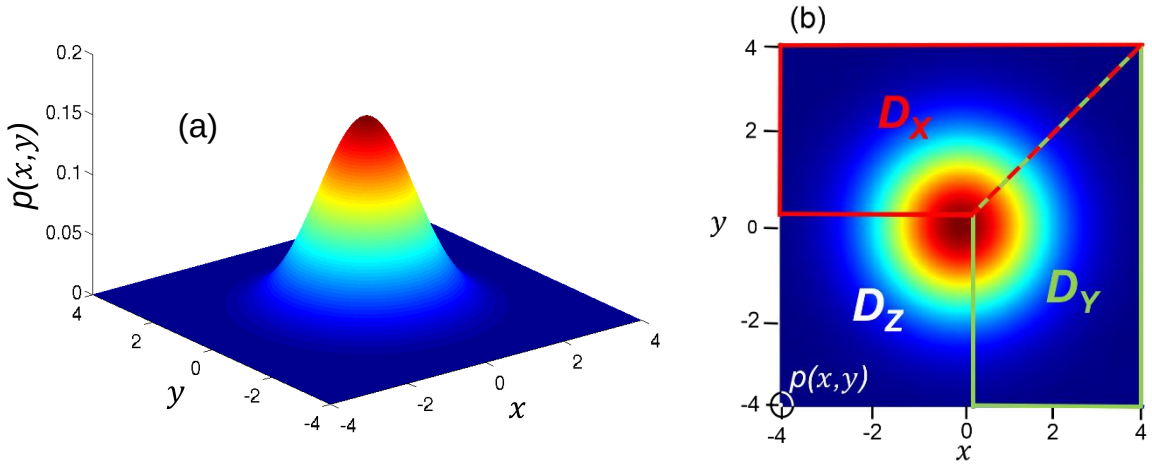

Fig. 3. Distribution and definition of the thresholds for a three-phase electrode: the Gaussian field follows a normal bivariate distribution with probability density function *p(x,y)* (a) segmented with a domain partitioning shown in (b).

In order to get the synthetic microstructure, the bigaussian random field $G_{XY}(z)$ has to be segmented. The attribution of each voxel of $G_{XY}(z)$ to one of the three phases is carried out by the partitioning of the bivariate distribution $p(x,y)$. As illustrated in Fig. 3b, the distribution is divided in three cells or domains D_X, D_Y and D_Z associated to the three electrode phases. The sets *X*, *Y* and *Z* of the synthetic microstructure are thus obtained by thresholding $G_{XY}(z)$ as follows:

$$X = \{z; G_{XY}(z) \in D_X\} \;;\; Y = \{z; G_{XY}(z) \in D_Y\} \;;\; Z = \overline{X \cup Y} \tag{14}$$

The integrals of $p(x,y)$ on D_X and D_Y are equal to the volume fractions of *X* and *Y*:

$$\varepsilon_X = \int_{D_X} p(x,y)dxdy \text{ and } \varepsilon_Y = \int_{D_Y} p(x,y)dxdy \quad (15)$$

While the volume faction of the complementary phase *Z* is simply given by $\varepsilon_Z = 1 - \varepsilon_X - \varepsilon_Y$. As detailed in Lantuéjoul [39], the shape of the partitioning domains controls the contact surface between the phases. For example, angles of 120° at the triple point, defined as the intersection between the three domains, lead to an equal interfacial specific surface area between the phases (i.e. $S_p^{X,Y} = S_p^{X,Z} = S_p^{Y,Z}$).

To summarize, the model consists in the generation of two random fields $G_X(z)$ and $G_Y(z)$ corresponding to two of the three electrode phases. Then, the fields are combined and jointly thresholded on the basis of the domain partitioning of $p(x,y)$. This step is carried out in such way that the properties of the synthetic microstructure satisfy the volume fraction and the interfacial specific surface area measured on the real reconstruction. However, since the threshold cannot be constant for both phases, a bias is introduced in the model so that the covariance functions of the resulting microstructure are liable to not match perfectly the real ones. This error is minimized during the segmentation step by using a third constraint on the covariance functions.

Numerical implementations – The random fields $G_X(z)$ and $G_Y(z)$ are generated with the same procedure detailed in the previous section. In this case, two distinct Gaussian exponential correlation functions are used to fit the discrete values of $\rho_X(h)$ and $\rho_Y(h)$ with two different correlation lengths. The partitioning of $p(x,y)$ and the thresholding of $G_{XY}(z)$ are carried out by minimizing the errors *E* on the interfacial specific surface area $S_p^{i,j}$ and the covariance functions $C_i(z)$ between the synthetic and real microstructures:

$$E = \sum_{i,j\in\{X,Y,Z\};i\neq j} \frac{\left|S_p^{i,j} - S_{p\_real}^{i,j}\right|}{S_{p\_real}^{i,j}} + \sum_{0\le z\le z_{\max}} \sum_{i\in\{X,Y,Z\}} \frac{\left|C_i(z) - C_{i\_real}(z)\right|}{C_{i\_real}(z)} \quad (16)$$

This minimization is conducted by respecting the phase volume fractions. This sequence of the method is realized into an iterative loop that does not require the generation of a new random field. Indeed, the loop is only carried out after the generation of $G_{XY}(z)$ and only concerns the partitioning and thresholding of the random field. As a consequence, the time necessary to simulate a virtual three-phase material remains very short. Considering a volume of 15x15x15

μm^3 with a voxel size of 25 nm, the virtual microstructure of the studied three-phase electrode (for Cell-A: cf. Section 4.1) is created in ~230 seconds by using only one CPU (Intel© Xenon©), while, a time of several hours is needed to obtain the same microstructure with our sphere packing algorithm. For both cases, the memory usage is about ~3.5 Gigabytes.

Finally, without any constraints on the partitioning, the permutation of *X* and *Y* does not change the final synthetic microstructure. Therefore, only three combinations are possible to produce the synthetic microstructure depending on the choice of the complementary phase (i.e. *Z*=Ni, YSZ or Gas). As for the two-phase electrodes, no significant difference has been found whatever the selected combination.

3. Three-dimensional electrodes reconstructions and characterizations

3.1 Cells and materials

Two typical commercial SOCs have been investigated in the present work. The first cell, so-called Cell-A thereafter, consists of a dense 8%mol Y_2O_3-ZrO_2 (YSZ) electrolyte of 5 µm supported by a thick porous Ni-YSZ H_2 electrode of 260 µm. The active part of the O_2 electrode is a porous LSCF layer of 30 µm associated to a LSC current collector of 20 µm. A thin barrier layer of Ceria doped Gadolinium Oxide (CGO) is also added between the electrolyte and the O_2 electrode (3-4 µm). The H_2 electrode of the second cell, referenced as Cell-B in the following of the article, is also a Ni-YSZ cermet. It is composed of a thick current collector of 500 µm and an active functional layer of 10 µm. The Ni-YSZ bilayer is used as a structural support on which is layered the YSZ electrolyte (5 µm), the thin CGO barrier layer (2 µm) and the O_2 electrode in LSC (20 µm).

3.2 3D reconstructions by synchrotron X-ray nano-holotomography and FIB-SEM

In the present study, the model is validated on the electrodes reconstructions of two typical SOCs (Cell-A and Cell-B) that exhibit different materials and microstructures (leading a significant difference in their electrochemical behavior as reported in [56]). For this purpose, the electrodes active layers of both cells, in which the electrochemical reactions take place, have

been reconstructed by synchrotron X-ray holotomography [21,22]. The method, which has been adapted for the highly absorbent ceramic materials, presents the advantage to get 3D volumes with a large field of view (50 µm) and the ability to resolve details in the microstructure of few tens of nanometers [10]. The samples for the tomographic experiments have been prepared by milling cylindrical pillars in the cells with a Plasma Focused Ions Beam (PFIB) working with Xenon ions (Fig. 4a) [10]. The samples have then been scanned at ID16A Nano-Imaging beam line (ESRF) with selected X-ray energies of 17.05 KeV and 33.6 KeV for the O_2 and H_2 electrodes, respectively. The detailed protocol for data acquisitions and the procedure for the electrode reconstructions can be found in refs. [10,57,58]. The 3D images after reconstruction present a volume as large as ≈50 µm x 25^2 µm² x π = 98174 μm^3 with a voxel size of 25 nm (with π ≈3.1416 : cf. list of symbols) (Fig. 4b).

In complementarity with the X-ray reconstructions, the microstructure of O_2 electrode of Cell-B has been also characterized by FIB-SEM tomography (with a FEI Versa 3D microscope) according to the procedure already detailed in [16,59]. The FIB-SEM reconstruction exhibits a volume limited to 17^3=4913 μm^3 with a voxel size of 16.5 nm. Therefore, the FIB-SEM reconstruction presents a smaller volume but a higher resolution than its equivalent volume obtained by synchrotron X-ray tomography. This last characteristic of the FIB-SEM method is especially well adapted to describe the very fine microstructure of the O_2 electrode of Cell-B (cf. next section).

To complete the processing and obtain the final 3D microstructures, the raw images in gray levels have been filtered and segmented according to the methods detailed in [22]. The electrode reconstructions for Cell-A have been already presented in [57] while the electrode reconstructions for Cell-B have been especially acquired for the present study. The 3D rendering volumes after segmentation for both cells are displayed in Fig. 5 for the O_2 electrodes and Fig. 6 for the H_2 electrodes. It can be noticed that the O_2 electrode microstructure of Cell-A is significantly coarser than the one of Cell-B.

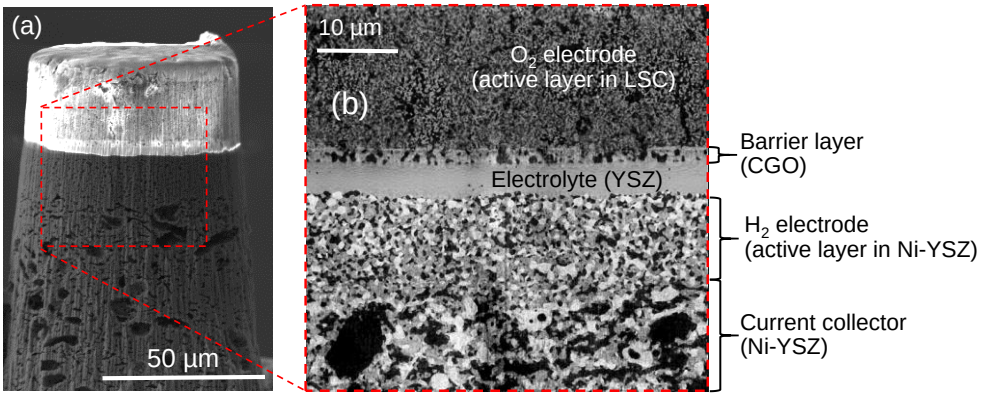

Fig. 4. Cell-B reconstruction: (a) Sample prepared by Xe PFIB for the tomographic experiment (Scanning Electron Image taken in secondary electron mode at 15 kV). (b) 2D cross section taken in the 3D reconstruction (image in grey levels with porosities in dark grey, Ni in bright grey and YSZ for the intermediate grey levels)

3.3 Microstructural properties measurements

The electrodes microstructure is assumed to be 'fully' characterized by a set of properties that can be measured on the 3D volumes. The procedures to compute these microstructural parameters have been already described in references [21,60]. Only the properties and the main steps of the procedures are listed and recalled hereafter:

(i) The phase volume fractions ε_i are directly given by the percentage of voxels belonging to the phase i while its contiguity δ_i is calculated by analyzing the phase connectivity from one side of the volume to the other [21].

(ii) The specific surface area S_p^i are deduced from the covariance functions as already presented in Section 2.1.

(iii) The continuous Phase Size Distributions (PSD) [60], also called granulometry, are computed using morphological openings with homothetic spheres as structuring elements as detailed by Serra [51].

(iv) The density of TPBls in the cermet, ξ_{TPB}, which is defined as the length of the Ni/YSZ/Gas intersections normalized by the domain volume, are calculated by identifying each voxel edges at the triple contacts. All the segments are then summed and a correction is introduced because of the domain cubic discretization [60]. In the present work, the density of 'active' TPBls is computed on the connected phases (cf. Table 2 and 3).

(v) The geometrical tortuosity τ_i^{geo} takes into account the fact that the mass or charge transport in one phase is hampered since the pathway for diffusion is not straight but sinuous and entangled [61,62]. This parameter is thus defined as the ratio of the effective pathway length ℓ^{eff} over the length of the sample ℓ and can be seen as a measure of the deviation from the shortest possible pathway:

$$\tau_i^{geo} = \ell^{eff} / \ell \tag{17}$$

This parameter is calculated by using 'centroid' path method [63-65]. For a given phase, the algorithm is based on the calculation of the center of mass within each 2D slices of the reconstruction along the in-plane direction of the flow. The effective length is then deduced by following the path from one centroid to the other.

(vi) The transport can be also hindered by some constrictions in the microstructure since the cross sections area for diffusion is not constant. This bottleneck effect is described through the constrictivity parameter that can be defined as follows [66]:

$$\beta_i = \left(r_{\min} / r_{\max}\right)^2 \tag{18}$$

By definition, the constrictivity β_i ranges between 0 and 1 (lower the parameter is, higher the constriction in the microstructure is). As proposed by Holzer et al. [66] and Gaiselmann et al. [67], the statistically averaged value for r_{min} is calculated by the simulation of the Mercury Intrusion Porosimetry (MIP) while r_{max}, which is defined as the radius of the phase size median, is determined with the continuous PSD.

This set of morphological parameters is finally complemented by the computation of the effective gas diffusivities or effective charge conductivities σ_i^{eff} for the percolated phases. Since the transport is limited by the complex microstructure, the effective conductivities σ_i^{eff} are lower than the intrinsic value for the dense material σ_i^{bulk}. The effect is taken into account through a microstructure-factor M_i defined as follows [66]:

$$M_i = \sigma_i^{eff} / \sigma_i^{bulk} \tag{19}$$

The ratio M_i is correlated to the electrode morphological parameters controlling the diffusional process. For instance, Stenzel et al. [14] have fitted on Ni-YSZ reconstructions a law which depends on the volume fraction, the geometrical tortuosity and constrictivity: $M_i = 2.08\left(\varepsilon_i^{1.62}\beta_i^{0.49}\right)/(\tau_i^{geo})^{2.26}$. It can be noticed that the microstructural factor is also classically used to express an 'apparent' tortuosity τ_i that encompasses both the transport

pathway (geometrical tortuosity) and the bottleneck effect (constrictivity): $M_i = \varepsilon_i / \tau_i^2$ [61,62]. In the present work, the effective conductivities have been determined by using a classical homogenization technique [21]. For each conducting phase, the equation for diffusion are solved in the digitized domain with the Finite Element Method (FEM). The effective conductivity is then deduced from the numerical analysis by equating the macro homogeneous flux to the average value computed from the FEM simulation.

In order to obtain good statistics, it is worth noting that the microstructural properties have to be quantified on the electrode Representative Volume Element (RVE), or if it is not possible, on several independent Stochastic Volume Elements (SVEs) extracted from the whole reconstructions [60,68,69]. In the present study, the RVE has been evaluated for each electrode with the method detailed in [21]. The density of TPBs, the volume fraction and the M-factors for each phase have been computed on several sub-volumes taken from the whole reconstructions. The RVE is reached when the standard deviation for each investigated parameter becomes negligible. Correspondingly, the requested number of SVE has been estimated in such a way that the standard deviation is very low after averaging on these independent volumes. Therefore, the microstructural parameters of the O_2 electrodes have been computed on a RVE estimated to ≈9x9x9 μm^3 for both cells [57] whereas the ones of the H_2 electrode of Cell-A have been calculated on a RVE evaluated to ≈15x15x15 μm^3 [57]. Since the H_2 electrode active layer of Cell-B has a thickness limited to 10 µm (Fig. 4), the computation of its microstructural properties have been carried out by averaging the data computed on 16 independent SVEs of ≈8.5x8.5x8.5 μm^3 (for which the standard deviation becomes negligible). All the properties including the effective conductivities have been calculated by keeping a voxel size (or element size for the FEM mesh) of 25 nm. As already discussed in [10], this discretization of the structure is adequate to describe correctly the morphological details in the microstructure and then to compute accurately its properties. Nevertheless, because of its very fine microstructure, it has been chosen to compute the properties of the O_2 electrode of Cell-B on the FIB-SEM volume by keeping a voxel size of 16.5 nm.

Moreover, both the covariance functions and the M-factors for each phase have been calculated in the three spatial directions. They have been found to be very close to each other meaning that the electrodes can be considered as an isotropic medium. As a consequence, all the electrodes properties have been averaged on the three spatial directions. All the parameters for both Cell-A and Cell-B are given in Table 1, 2 and 3 for the O_2 and H_2 electrodes.

4. Validation of the random field model on 3D reconstructions

4.1 Validation for the two-phase O_2 electrodes

The model for the two-phase materials has been validated on the LSCF and LSC O_2 electrodes of Cell-A and Cell-B. The 3D rendering volumes of the real and synthetic microstructures are compared in Fig. 5. As a first approach, the visual inspection of the 3D volumes for both electrodes reveals that the virtual microstructures seem to mimic quite perfectly the real ones. Therefore, it seems that the model would be able to describe accurately the coarse microstructure of Cell-A as well as the finer microstructure of Cell-B. As illustrated in Fig. 6a, this first statement is confirmed by the very good agreements between the covariance functions calculated on the synthetic volumes and the tomographic reconstructions. As it was expected, this result highlights in one hand the possibility to compute accurately the correlation $\rho_X(h)$ with eq. (10), and in the other hand, to have a good fit of $\rho_X(h)$ with the exponential correlation function.

To go further in the model validation, the cumulative PSD and all the key electrode microstructural parameters of the virtual electrodes have been determined in the same conditions than the data computed with the tomographic reconstructions (i.e. for the same RVE and voxel size). As shown in Table 1, a very good agreement is achieved for all the parameters calculated for both electrodes. Indeed, the relative errors listed in Table 1 remain restricted in a range of few percent. For instance, the disagreement in respect of the electrode specific surface area, which is a crucial parameter controlling the electrode kinetic rate for the oxygen incorporation [70], does not exceed 5% for both cells. Actually, the highest mismatch is found for the geometrical tortuosity and the constrictivity factor related to the pore phase of Cell-B. In this case, the error on these two parameter reaches values of around +/-10%. It can be noticed that the mismatch between the virtual and real volumes arises for the phase that exhibits the finest microstructure characterized by the lowest mean particle size diameter and phase volume fraction. Therefore, for the two-phase electrode, the model yields the highest discrepancies on the geometrical tortuosity and constrictivity factor for the finest electrode microstructure.
It can be also remarked that the M-factor presents an error ranging between +/-5% and +/-10% whatever the investigated electrode phase (Table 1). Indeed, this parameter combines the errors

on the phase volume fraction, the geometrical tortuosity and constrictivity as discussed previously. Nevertheless, despite this discussion on its limitation, it worth underlining that the model is able to statistically reproduce the main O_2 electrode microstructural properties with a high level of confidence.

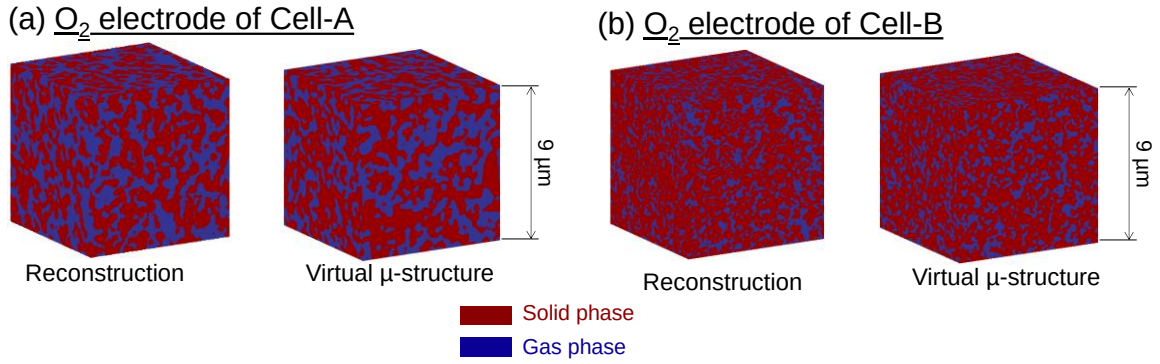

Fig. 5. Visual comparison between the synthetic microstructures and the reconstructed volumes for the O_2 electrodes of (a) Cell-A and (b) Cell-B.

Table 1
Microstructural properties for the O_2 electrodes of Cell-A and Cell-B computed on the tomographic reconstructions and the synthetic volumes.

O_2 electrode of Cell-A													
		Gas phase						**Solid phase (LSCF)**					
Properties	S_p μm^{-1}	δ (%)	ε (%)	$d_p^{(*)}$ (µm)	τ^{geo} (-)	β (-)	M-factor (-)	δ (%)	ε (%)	$d_p^{(*)}$ (µm)	τ^{geo} (-)	β (-)	M-factor (-)
Real µ-structure	3.80	99.96	43.64	0.26	1.22	0.10	0.194	99.99	56.36	0.32	1.34	0.11	0.289
Virtual µ-structure	3.78	99.94	43.61	0.27	1.23	0.11	0.185	99.98	56.39	0.32	1.46	0.12	0.319
Error	~0%	~0%	~0%	+4%	~0%	+4%	-5%	~0%	~0%	~0%	+9%	+6%	+10%
O_2 electrode of Cell-B													
		Gas phase						**Solid phase (LSC)**					
Properties	S_p μm^{-1}	δ (%)	ε (%)	$d_p^{(*)}$ (µm)	τ^{geo} (-)	β (-)	M-factor (-)	δ (%)	ε (%)	d_p (µm)	τ^{geo} (-)	β (-)	M-factor (-)
Real µ-structure	6.28	99.76	28.83	0.12	2.27	0.23	0.078	100	71.17	0.22	1.31	0.31	0.474
Virtual µ-structure	5.97	99.47	28.85	0.13	2.03	0.26	0.084	100	71.15	0.24	1.22	0.33	0.497
Error	-5%	~0%	~0%	+8%	-11%	+13%	+7%	~0%	~0%	+9%	-7%	+6%	+5%

(*) mean phase diameter taken from the PSD.

Finally, as shown in Fig. 6c and 6d for both cells, a good agreement is also observed between the cumulative PSDs of the virtual and real electrodes. It is worth mentioning that these curves characterize all the morphological details of the microstructure at different length scales. From that point of view, they integrate all the errors for the morphological parameters listed in Table 1. Therefore, the PSD plots can be seen as the toughest criteria to validate the model. Since the mismatch with the real electrodes is rather limited for both cells, it is claimed that the

microstructure generated with truncated Gaussian random field is fully representative of the two-phase electrode materials.

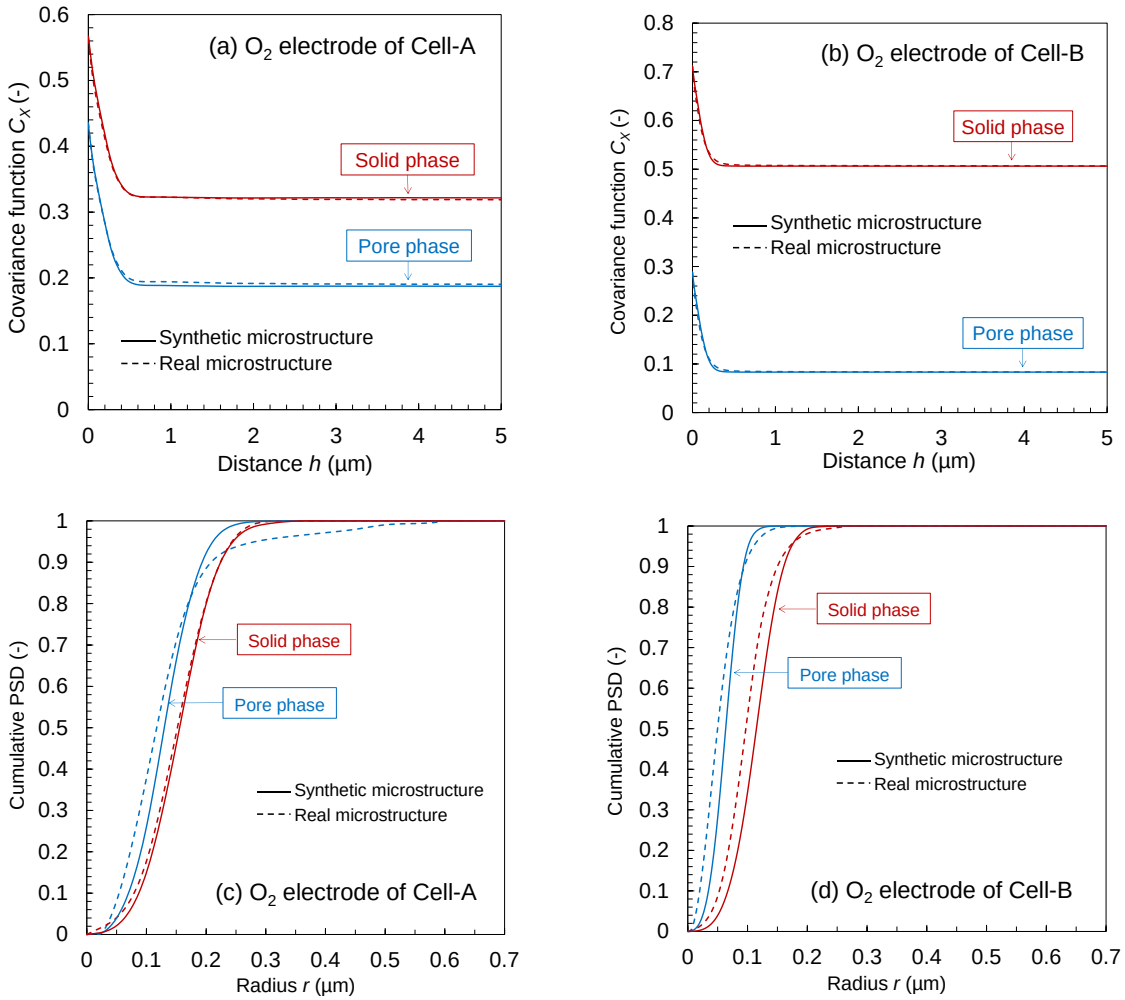

Fig. 6. Comparison between the synthetic and real O_2 electrode microstructures in respect of (a,b) the covariance functions and (c,d) the cumulative PSDs for both Cell-A and Cell-B.

4.2 Validation for the three-phase H_2 electrodes

The Ni-YSZ synthetic microstructures has been generated with the two independent random fields G_X and G_Y related to the two solid phases and the porosity as the complementary set. As already mentioned, no large difference in terms of representativeness has been found whatever the considered combination. The 3D rendering volumes of the synthetic microstructures are compared to the Ni-YSZ cermet reconstructions in Fig. 7. As for the LSCF or LSC electrode, the visual inspection indicates that the model would be able to describe correctly the more complex microstructure of the three-phase electrodes. This preliminary observation is also

supported by the good agreement found between the covariance functions of the real and synthetic microstructures (Fig. 8a and 8b).

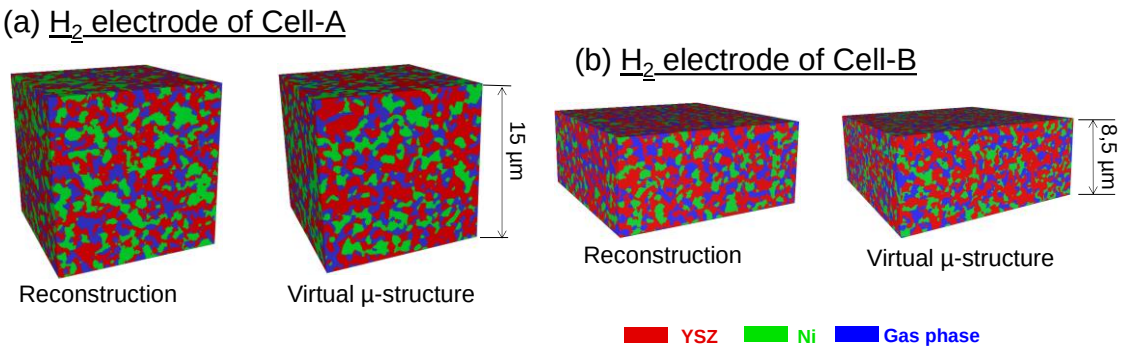

Fig. 7. Visual comparison between the synthetic microstructures and the reconstructed volumes for the H_2 electrodes of (a) Cell-A and (b) Cell-B.

To check more precisely the model representativeness, the microstructural properties of the synthetic volume have been compared to the real values in Table 2 and 3. As a general matter, a rather good accordance is found for all the parameters. More specifically, it can remarked that the model is able to reproduce accurately the density of TPBs which is of central importance as it controls the efficiency of the Ni-YSZ electrode [8]. Indeed, the error on the density of TPBs is less than +/-2.5% for the two studied cells. Moreover, the model is also able to capture correctly the electrodes specific surface areas for both electrodes with a mismatch that does not exceed +/-2%. Actually, the highest discrepancy arises for the transport properties of the pore and Ni phases of Cell-A and Cell-B. In this case, the errors on the M-factor ranges between 20-25% while the one for the YSZ phase of both electrodes remains negligible (≤1%). This noticeable discrepancy on the microstructural factor for the Ni and pore phases is clearly related to the error on the constrictivity parameter (cf. Table II). This mismatch on the constrictivity seems to be correlated with the phases that exhibit the lowest volume fraction (<30% for the Ni and pores and >45% for the YSZ). In other words, it appears that the model is able to reproduce accurately the metric properties (i.e. volume fractions, specific surface areas, mean phase diameters and density of TPBs), whereas a higher discrepancy on the topological parameters (i.e. constrictivity and tortuosity) is detected for the phases with a low volume fraction (cf. Ni phase in Table 2 and 3). As the topological properties are related to the connectivity [82], a large variation in their values can be expected when the volume fractions get closer to the percolation threshold. This remark could explain the apparent correlation between the error on

tortuosity and constrictivity for low phase volume fractions. However, some authors [83] have proved, for some random spatial structures, that there does not exit any direct link between the percolation threshold and its topology described by the Euler-Poincaré characteristic. From this point of view, it appears that further investigations are still needed to better understand the evolution of the electrode topology close to the percolation limit. Nevertheless, as a general comment for the three-phase electrode, it turns out that the model exhibits a limitation to reproduce with a high level of confidence a microstructure composed of very high constrictive phases associated with low volume fraction.

The cumulative PSDs are plotted in Fig. 8c and 8d for Cell-A and Cell-B. There is a relatively good agreement between the curves. As expected, the highest discrepancies arise for the Ni and pore phases of Cell-A and Cell-B. In this case, the curves for the real microstructure are more widespread than the ones for the synthetic volume. It means that the Ni and pore phases present a large distribution of particle lengths which is well correlated with their low constrictivity parameters. This results highlight the model limitation to model perfectly the high constriction effect associated with a large distribution of particle size. Nevertheless, it is worth mentioning that this limitation of the model remains acceptable for the investigated SOCs electrodes (in the worst case, the error on the microstructural factor does not exceed 25% for Cell A and 24% for Cell-B: cf. Table 2 and 3). As a consequence, despite the limitation on the constrictivity factor, it can be then concluded that the adapted plurigaussian random field model is able to simulate accurately the main electrode properties, and then to provide a realistic and representative Ni-YSZ synthetic microstructure.

Table 2
Microstructural properties for the H_2 electrodes of Cell-A computed on the tomographic reconstruction and the synthetic volume.

H_2 electrode of Cell-A														
	Gas phase							**Electronic conducting phase (Ni)**						
Properties	S_p μm^{-1}	δ (%)	ε (%)	$d_p^{(*)}$ (µm)	τ^{geo} (-)	β (-)	M-factor (-)	S_p μm^{-1}	δ (%)	ε (%)	$d_p^{(*)}$ (µm)	τ^{geo} (-)	β (-)	M-factor (-)
Real µ-structure	2.67	94.74	28.04	0.28	1.67	0.09	0.030	2.30	97.45	27.88	0.33	1.75	0.08	0.041
Virtual µ-structure	2.64	99.43	28.14	0.28	1.62	0.11	0.036	2.32	99.21	27.78	0.34	1.70	0.10	0.051
Error	-1%	+4%	~0%	~0%	-3%	+22%	+21%	+1%	+2%	~0%	+3%	-3%	+25%	+25%
	Ionic conducting phase (YSZ)							**Density of TPBls (Ni/YSZ/gas contact lengths)**						
Properties	S_p μm^{-1}	δ (%)	ε (%)	$d_p^{(*)}$ (µm)	τ^{geo} (-)	β (-)	M-factor (-)	ξ_{TPBls} $^{(**)}$ (μm^{-2})						
Real µ-structure	3.68	99.78	44.08	0.28	1.43	0.13	0.189	4.78						
Virtual µ-structure	3.65	99.94	44.08	0.29	1.43	0.13	0.190	4.73						
Error	-1%	~0%	~0%	+3%	~0%	~0%	~0%	-1%						

$^{(*)}$ mean phase diameter taken from the PSD. $^{(**)}$ density of 'active' TPBls computed on the connected phases.

Table 3

Microstructural properties for the H_2 electrodes of Cell-B computed on the tomographic reconstruction and the synthetic volume.

H_2 electrode of Cell-B														
	Gas phase							Electronic conducting phase (Ni)						
Properties	S_p μm^{-1}	δ (%)	ε (%)	$d_p^{(*)}$ (μm)	τ^{geo} (-)	β (-)	M-factor (-)	S_p μm^{-1}	δ (%)	ε (%)	$d_p^{(*)}$ (μm)	τ^{geo} (-)	β (-)	M-factor (-)
Real μ-structure	2.94	94.23	26.55	0.24	1.74	0.39	0.021	2.46	92.81	24.13	0.28	1.81	0.34	0.018
Virtual μ-structure	2.87	98.65	26.80	0.25	1.66	0.45	0.026	2.41	97.75	24.82	0.28	1.74	0.41	0.021
Error	-2%	+4%	+1%	+4%	-4%	+15%	+24%	-2%	+5%	+2%	~0%	-4%	+21%	+17%
	Ionic conducting phase (YSZ)							Density of TPBls (Ni/YSZ/gas contact lengths)						
Properties	S_p μm^{-1}	δ (%)	ε (%)	$d_p^{(*)}$ (μm)	τ^{geo} (-)	β (-)	M-factor (-)	$\xi_{TPBls}^{(**)}$ (μm^{-2})						
Real μ-structure	3.42	99.92	49.55	0.31	1.14	0.44	0.243	6.20						
Virtual μ-structure	3.45	99.98	48.38	0.31	1.13	0.47	0.246	6.07						
Error	+1%	~0%	-2%	~0%	-1%	+7%	+1%	-2%						

(*) mean phase diameter taken from the PSD. (**) density of 'active' TPBls computed on the connected phases.

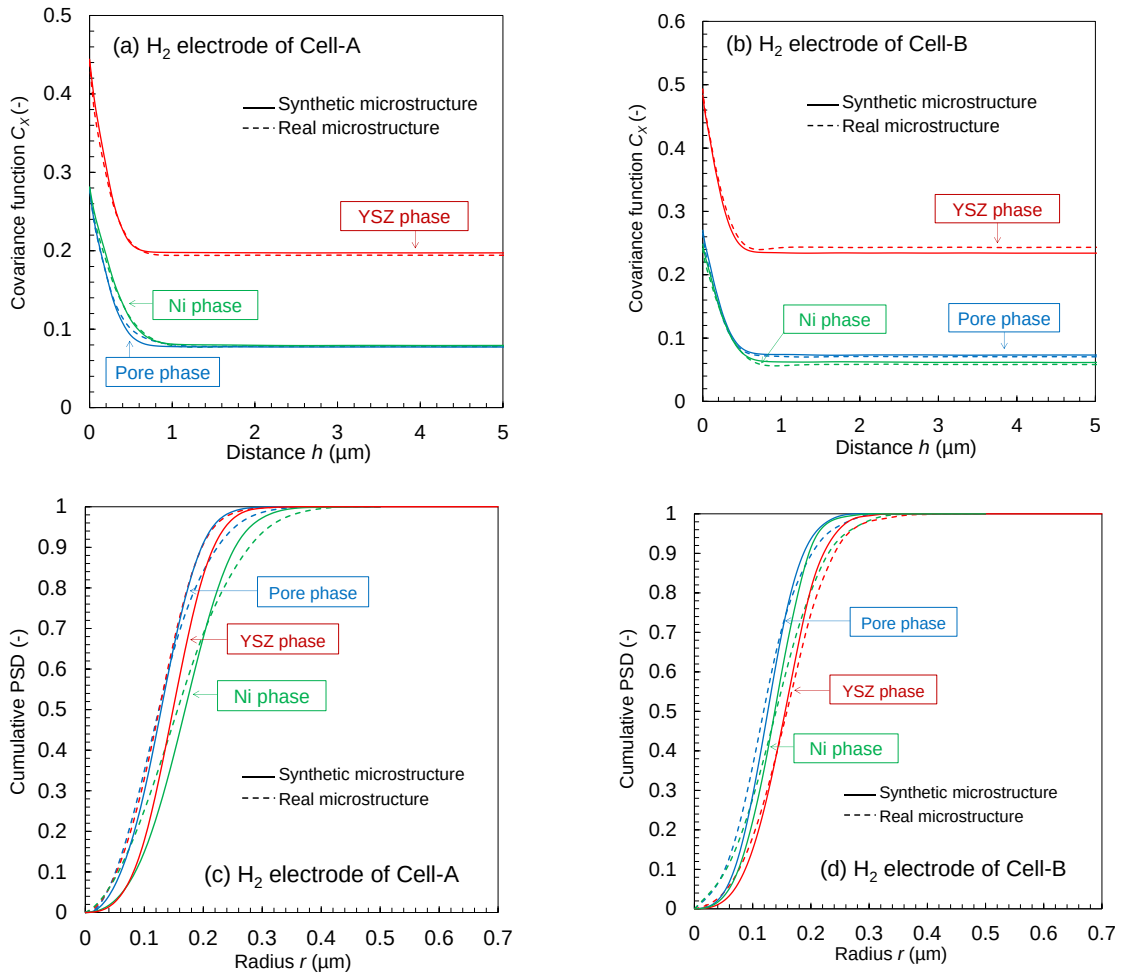

Fig. 8. Comparison between the synthetic and real H_2 electrode microstructures in respect of (a,b) the covariance functions and (c,d) the cumulative PSDs for both Cell-A and Cell-B.

In ref. [71], the authors have investigated the representativeness of the model proposed by Abdallah et al. [44] who considered an alternative method based on two underlying independent Gaussian random fields with two constant thresholds for the segmentation. The validation was performed on the same Ni-YSZ electrode reconstruction of Cell-A. The deviation from the real microstructural properties was significantly higher than the one reported in Table 2. For instance, the error on the density of TPBs and the constrictivity for the Ni phase reaches 11% and 38%, respectively [71]. Therefore, the proposed model based on an adjusted partitioning of the bigaussian field G_{XY}, is more accurate to simulate representative microstructures, and hence it can be seen as an improved method regarding the SOC application.

5. Discussion: model flexibility to various electrode microstructures

With the present validated numerical tool, different synthetic microstructures could be generated by changing the model input parameters. If considering the 3D reconstructions as the reference electrode, the set of synthetic volumes could be used to establish the microstructural relationships for the classical SOC electrodes. For instance, the effect of phase volume fractions can be easily investigated by changing the random field thresholding. Moreover, in order to investigate a finer or a coarser microstructure, the mean diameter of each phase can be tuned by changing its correlation length in the expression of $\rho_i(h)$ (cf. eq. (12)). This kind of sensitivity analysis can be used for a numerical optimization of the SOC electrode microstructures in order to provide guidelines for the cell manufacturing. Nevertheless, aside from this classical optimization, the relevance of the 3D microstructure model must also stand in its capacity to generate a large variety of innovative electrode architectures. In the following, the model flexibility is illustrated and discussed on different examples of promising electrode designs.

5.1 Impact of domain partitioning

As mentioned in Section 2.2, the contact surface areas between the phases in the three-phase electrode depend on the domain partitioning of the bivariate distribution. This property of the model can be useful to control the ‘coverage rate’ of one phase to the other, and hence, to adapt the interfacial specific surface areas between the electrode phases. This model property is

illustrated on Fig. 9: by changing the domain partitioning, the specific surface areas can be easily tuned by keeping the same phase volume fractions and phase characteristic lengths. As expected, the density of TPBls is maximal when the three interfacial specific surface areas are equal (Fig. 9). Nevertheless, knowing that the volume fractions and characteristic lengths are not modified, it can be remarked that the density of TPBls is not strongly affected by changing the domain partitioning. Advantage could be taken of this model specificity regarding the microstructural optimization. Indeed, as an illustration for the LSCF/CGO composite, the maximization of the LSCF/gas interface by keeping a sufficiently high density of TPBls would be necessary to promote the oxygen adsorption and incorporation [10]. Correspondingly for the Ni/YSZ cermet operated in electrolysis mode, it could also be interesting to increase the Ni/gas interface area to favor the suspected limiting step of steam adsorption on the Ni surface [2].

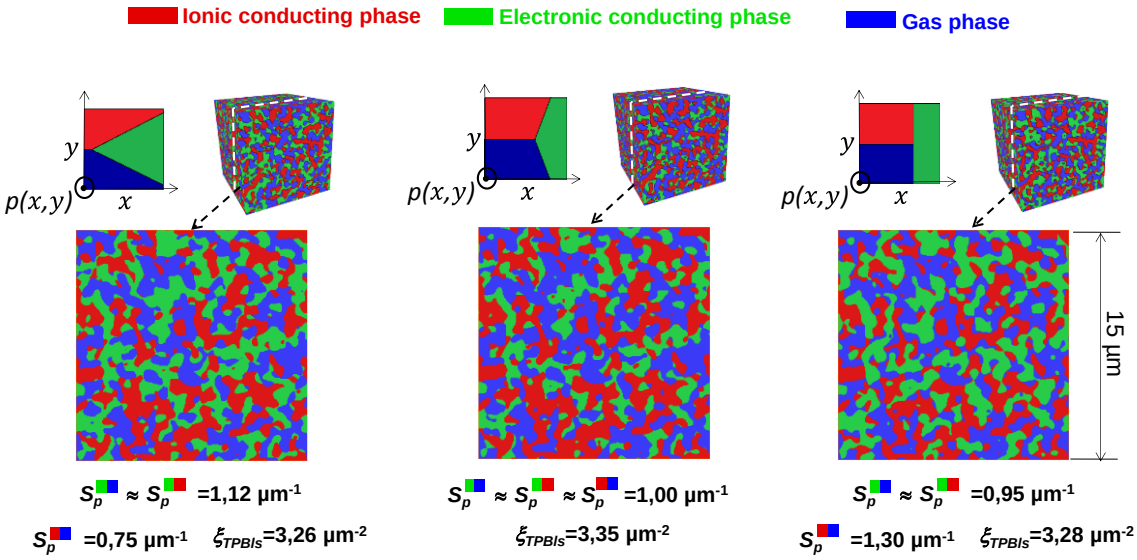

Fig. 9. Impact of domain partitioning for a composite electrode. The 'coverage rate' between the phases can be tuned to control the specific surface areas and density of TPBs (simulated microstructure with the same volume fraction for each phase).

Furthermore, the particular situation of constant parallel thresholds leads to divide the domain in three horizontal cells resulting in a microstructure with one intermediate phase that surrounds the other (Fig. 10). By taking advantage of this model specificity, it becomes possible to model the electrodes prepared by infiltration which have the potentiality to be the next generation of functional active layers replacing the classical composite [72]. Indeed, depending of the manufacturing process, the infiltration results in a continuous thin film deposited on an electrode scaffold [5,73]. As shown in Fig. 10, this particular materials architecture can be easily modeled by reducing the volume fraction of the intermediate phase with the partitioning in three parallel strips of the bivariate distribution.

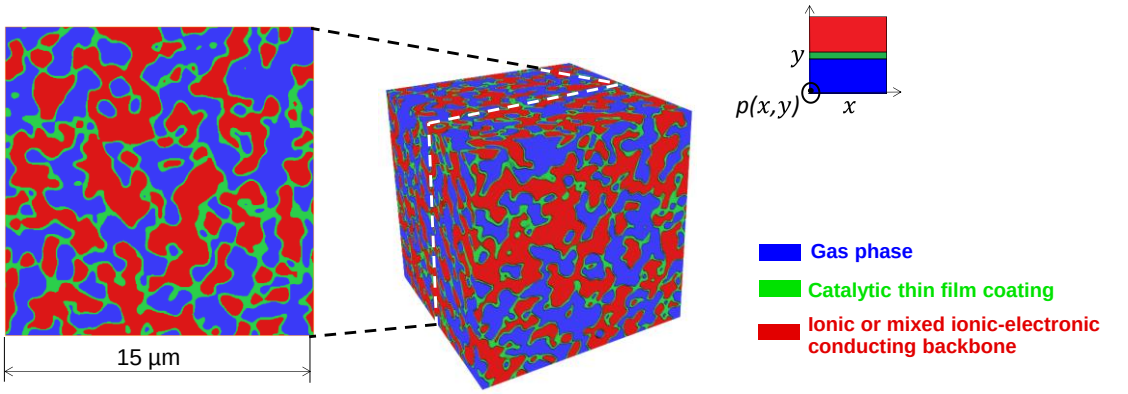

Fig. 10. Simulation of a thin film coating impregnated onto the surface of the electrode backbone (simulated microstructure with: ε=0.41 for the ionic conducting scaffold, ε=0.19 for the catalytic coating).

5.2 Introduction of a local thresholding: illustration on the graded electrodes

With the random field model, spatial heterogeneities can be introduced in the microstructure with a threshold that depends on the local position in the material. This model feature offers the possibility to generate specific architectures for optimizations by material design. In this frame, the Functionally Graded Materials (FGM), which exhibit a spatial distribution in the composition and/or in the structure, are nowadays widely studied as advanced engineering materials [74]. The concept of FGM has been applied to the SOC electrodes in an attempt to enhance the cell efficiency and reliability [75,76]. With a gradient in composition and/or particle size for both electronic and ionic conducting phases, it has been shown that the electrode performances may be improved by optimizing the ohmic losses in the active layer [77,78]. Besides, by mitigating the thermal expansion mismatch with the electrolyte, it has been shown that the graded electrodes present an enhanced mechanical stability [79]. Nevertheless, the best compromise between the mechanical robustness and electrochemical efficiency needs to be identified [78].

As an illustration of the local thresholding for the SOC application, the graded electrodes have been simulated with the model. For the two phase materials, a gradient in composition can be easily introduced in the microstructure by considering a threshold that evolves continuously along the thickness of the active layer (Fig. 11a). For the composite electrodes, the microstructure should exhibit two opposite compositional gradients for the electronic and ionic

conducting phases in order to maximize the collection of both electronic and ionic currents [78]. This structure can be simulated by using a space dependent partitioning of the bivariate distribution in order to get the targeted local electrode composition. Moreover, this mapping can be done by controlling the angle around the triple point to optimize the interfacial specific surface areas (cf. previous section). For a sake of clarity, the evolution of domain partitioning is illustrated in Fig. 11b for two constant thresholds. As expected, the resulting microstructure presents two continuous and opposite gradients for the ionic and electronic conducting phases (Fig. 11c) that are assumed to be well representative of real graded electrodes. Thanks to the model flexibility, the compositional gradients in association with the local morphological characteristics such as interfacial surface area are liable to be optimized.

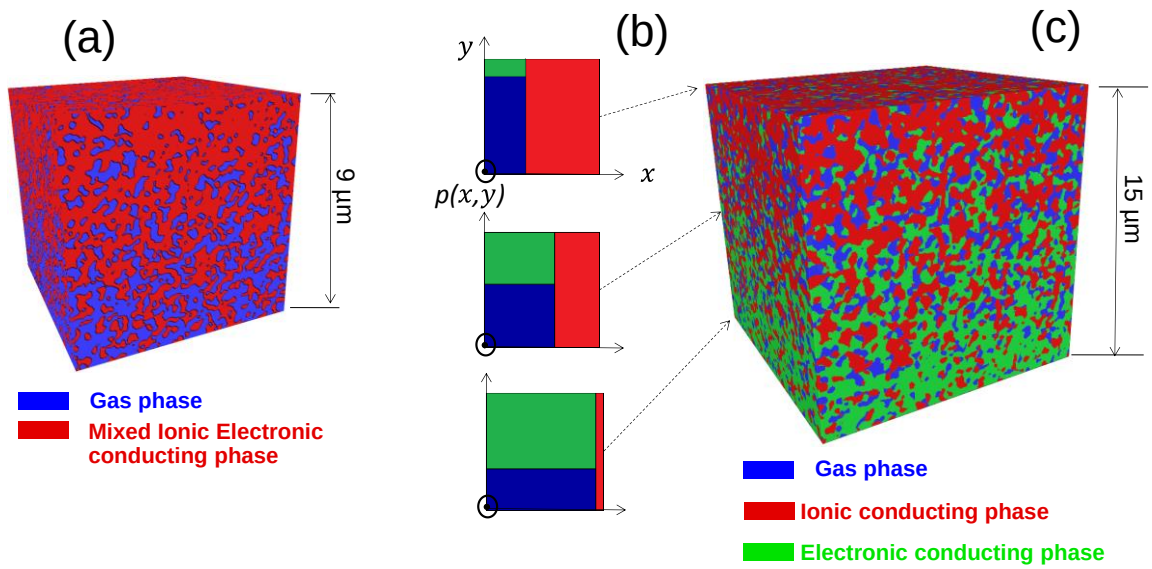

Fig. 11. Graded electrodes simulated with the local thresholding: (a) 3D rendering volume for a two-phase electrode, (b) Evolution of the domain partitioning: illustration of the thresholding maps taken at three different locations along the electrode thickness and (c) 3D rendering volume for a three-phase electrode.

5.3 Introduction of a multi-correlation length: impact on interfacial roughness

The morphology of the solid/solid or gas/solid interface plays a major role in the SOC electrode efficiency. Indeed, a high surface exchange between the phases is generally required to favor the reactions of mass and/or charge transfers. Aside from the classical ceramic manufacturing routes, various deposition techniques such as the Electrostatic Spray Deposition (ESD) [6] have been recently used to control the electrode surface morphology. For example, the ESD has

allowed to produce LSCF nanostructured porous coatings for the O_2 electrode with a high surface area [80].

In order to reproduce such kind of electrodes, it can be interesting to produce virtual microstructures by controlling the local topology of the gas/solid interface. This can be achieved with the random field model by introducing a second correlation length ℓ^* related to the electrode local roughness. This possibility has been investigated for the O_2 electrode. The method is based on the generation of two random fields, $G_{X,\ell}(z)$ and $G_{X^*,\ell^*}(z)$, containing the information on the characteristics lengths at the 'microscopic' and 'nanoscopic' scales, ℓ and ℓ^*, respectively. Typically, the characteristic length ℓ of the microstructure is around 0.25-0.75 µm while the dimension of the local roughness ℓ^* could be in the range of few tens of nanometers [80]. In practice, $G_{X,\ell}(z)$ and $G_{X^*,\ell^*}(z)$ are combined in a bigaussian field and then segmented considering a specific diagonal domain partitioning defined by the threshold $G_X + G_{X^*} = \lambda$. This domain partitioning allows to give the same weight for the characteristics of $G_{X,\ell}(z)$ and $G_{X^*,\ell^*}(z)$ in the final synthetic microstructure. It is equivalent to add the two fields and used a constant threshold as follows:

$$G_{solid}(z) = G_{X,\ell}(z) + G_{X^*,\ell^*}(z) \quad \text{with } \ell^* < \ell \text{ and } \varepsilon_{solid} = P\{G_{solid}(z) \geq \lambda\} \tag{20}$$

As the method is based on the sum of two independent random fields $G_{X,\ell}(z)$ and $G_{X^*,\ell^*}(z)$ associated to their correlation functions $\rho_{X,\ell}(z)$ and $\rho_{X^*,\ell^*}(z)$, it is also equivalent to the generation of one single field $G_{XX^*,\ell,\ell^*}(z)$ defined by the correlation $\rho_{XX^*,\ell,\ell^*}(z) = \rho_{X,\ell}(z) + \rho_{X^*,\ell^*}(z)$. Note the procedure leads to add some few small disconnected inclusions in the phases that are removed by simple morphological operation [51].

To illustrate the method, the O_2 electrode microstructures obtained with one and two correlation lengths have been generated and compared in Fig. 12a and 12b. In order to make the comparison relevant, it is worth noting that the two microstructures have been generated in such a way that they present the same phase volume fraction and the same mean particle size. As expected, the microstructure which combines the two correlation lengths presents a much higher surface roughness than the one obtained with the classical method. Indeed, the electrode specific surface area is increased from 3.89 μm^{-1} for the classical microstructure to 5.12 μm^{-1} for the

second one. This evolution is in good agreement with the PSD of the solid phase plotted in Fig. 12c: the microstructure obtained with two correlation lengths exhibits a dissymmetry in the distribution due to the appearance of small particles related to the surface roughness. This results highlight the flexibility of the method to control the morphology of the electrode interfaces.

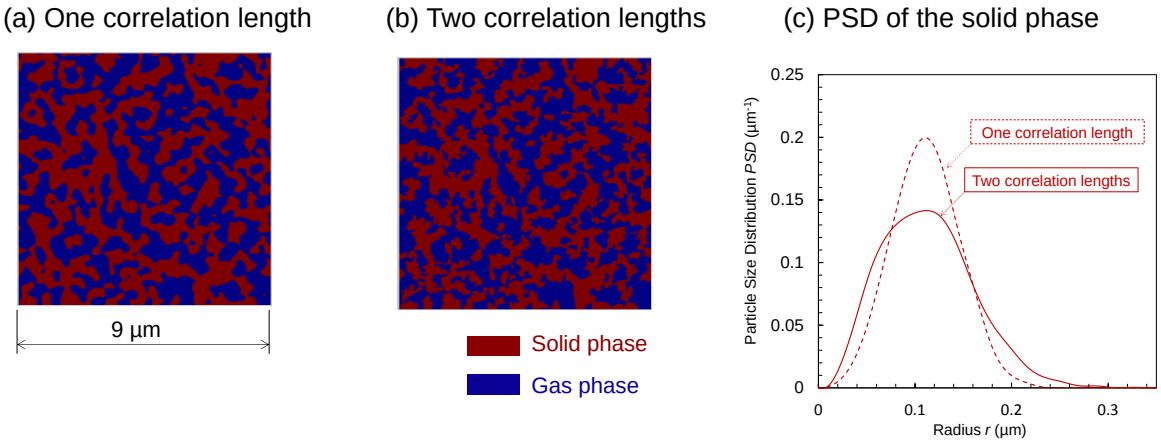

Fig. 12. 2D slices taken in the 3D synthetic volume for a two-phase electrode simulated with: (a) one correlation length and (b) two correlation lengths. (c) PSD plots for the two microstructures. Both electrodes have been simulated so that they have the same phase volume fraction (ε_{solide}=0.5) and mean phase diameter (d_p=0.2 µm).

6. Conclusion

An original 3D stochastic model, based on the truncated plurigaussian random fields, has been adapted to simulate the complex microstructure of SOC electrodes. To improve the relevance of the method regarding to the application, the model includes a generalization consisting in an *Ad hoc* partitioning of the combined random fields. A special attention has also been paid to the numerical implementation in order to generate the electrode virtual microstructure in a very short time. This criterion is of central importance for forthcoming studies devoted to the microstructural optimization or to the assessment of the complex relationships linking the morphological electrode properties.

The representativeness of the virtual microstructures has been checked on several synchrotron X-ray and FIB-SEM tomographic reconstructions obtained on typical LSCF, LSC and Ni-YSZ electrodes. The validation step has been carried out by comparing a set of relevant electrode morphological properties as well as the phase effective conductivities or diffusivities. It has

been found that the model is able to reproduce accurately the density of TPBs and the specific surface areas which are the main parameters controlling the reaction kinetic rates in the electrodes. For both of this microstructural properties, the mismatch between the synthetic material and the real reconstruction do not exceed a few percent whatever the tested electrode. Although the model fails to reproduce perfectly very high constrictive phases, the characteristic parameters controlling the mass and charge transport in the virtual microstructures have been found to be in rather good agreement with the properties of the real electrodes. As a general matter, it was inferred from this analysis that the synthetic media mimic correctly the complex microstructure of typical SOC electrodes.

Finally, the model flexibility to simulate different types of SOC microstructural architectures has also been illustrated on different examples. Aside from the classical properties such as the volume fractions or the characteristic lengths of the phases, a specific domain partitioning of the bigaussian random field allows controlling the coverage rate of one solid phase to the other. This characteristic of the model is particularly useful to generate SOC electrode prepared by infiltration resulting in a uniform and continuous thin layer covering a scaffold. With a local thresholding depending on the position, continuous graded electrodes can be also produced. Finally, the model offers the possibility to introduce different correlation lengths for each phase in order to control the local topology of the interfaces. All these cases illustrate the model capability to be adapted to the different kind of promising electrode designs for further numerical microstructural optimizations.

Acknowledgments

The research leading to these results has received funding from European Horizon 2020 - Research and Innovation Framework Programme (H2020-JTI-FCH-2015-1) under grant agreement n° 699892 (ECO project). The work has also been partially supported by the French National Research Agency (ANR) (DJANGO project).

References

[1] S.C. Singhal and K. Kendall, "High Temperature Solide Oxide Fuel cells, Fundamental, Design and Applications", Elsevier, 2003.

[2] A. Godula-Jopek, "Hydrogen Production by Electrolysis", Wiley, 2015.

[3] C. Graves, S.D. Ebbesen, S.H. Jensen, S.B. Simonsen, M.B. Mogensen, Nature Materials, 14 (2015) 239-244.

[4] N.H. Menzler, F. Tietz, S. Uhlenbruck, H.P. Buchkremer, D. Stöver, J. Mater. Sci., 45 (2010) 3109-3135.

[5] D. Ding, X. Li, S.Y. Lai, K. Gerdes, M. Liu, Energy Environ. Sci., 7 (2014) 552-575.

[6] R.K. Sharma, M. Burriel, L. Dessemond, V. Martin, J.-M. Bassat, E. Djurado, J. Power Sources, 316 (2016) 17-28.

[7] A.V. Virkar, J. Chen, C.W. Tanner, J.-W. Kim, Solid State Ionics, 131 (2000) 189-198.

[8] E. Lay-Grindler, J. Laurencin, G. Delette, J. Aicart, M. Petitjean, L. Dessemond, Int. J. of Hydrogen Energy, 38 (2013) 6917-6929.

[9] A. Bertei, B. Nucci, C. Nicolella, Chemical Engineering Science, 101 (2013) 175-190.

[10] M. Hubert, J. Laurencin, P. Cloetens, J.C. da Silva, F. Lefebvre-Joud, P. Bleuet, A. Nakajo, E. Siebert, Solid State Ionics, 294 (2016) 90-107.

[11] A.M. Gokhale, S. Zhang, M. Liu, J. Power Sources, 194 (2009) 303-312.

[12] X. Liu, C. Martin, G. Delette, J. Laurencin, D. Bouvard, T. Delahaye, J. Power Sources, 196 (2011) 2046-2054.

[13] D. Chen, H. He, D. Zhang, H. Wang, M. Ni, Energies, 6 (2013) 1632-1656.

[14] O. Stenzel, O. Pecho, L. Holzer, M. Neumann, V. Schmidt, AIChE Journal, 62(5) (2016) 1834-1843.

[15] J.R. Wislon, W. Kobsiriphat, R. Mendoza, H.Y. Chen, J.M. Hiller, D.J. Miller, K. Thorton, P.W. Voorhees, S.B. Adler, S.A. Barnett, Nat. Mater. 5 (2006) 541–544.

[16] N. Vivet, S. Chupin, E. Estrade, T. Piquero, P.L. Pommier, D. Rochais, E. Bruneton, J. Power Sources 196 (2011) 7541–7549.

[17] L. Holzer, B. Münch, B. Iwanschitz, M. Cantoni, T. Graule, J. Power Sources 196 (2011) 7076–7089.

[18] K.N. Grew, Y.S. Chu, J. Yi, A.A. Peracchio, J.R. Izzo, Y. Hwu, F. De Carlo, W.K. Chiu, J. Electrochem. Soc. 157 (6) (2010) B783–B792.

[19] P.R. Shearing, R.S. Bradley, J. Gelb, F. Tariq, P.J. Withers, N.P. Brandon, Solid State Ionics 216 (2012) 69–72.

[20] J.S. Cronin, Y.C.K. Chen-Wiegart, J. Wang, S.A. Barnett, J. Power Sources 233 (2013) 174–179.

[21] J. Laurencin, R. Quey, G. Delette, H. Suhonen, P. Cloetens, P. Bleuet, J. Power Sources, 198 (2012) 182-189.

[22] J. Villanova, J. Laurencin, P. Cloetens, P. Bleuet, G. Delette, H. Suhonen, F. UsseglioViretta, J. Power Sources 243 (2013) 841–849.

[23] J.R. Wilson, J.S. Cronin, A.T. Duong, S. Rukes, H.-Y. Chen, K. Thornton, D.R. Mumm, S.A. Barnett, J. Power Sources 195 (2010) 1829–1840.

[24] J.R. Wilson, J.S. Cronin, S.A. Barnett, Scripta Materialia, 65 (2011) 67-72.

[25] N. Vivet, S. Chupin, E. Estrade, A. Richard, S. Bonnamy, D. Rochais, E. Bruneton, J. Power Sources 196 (2011) 9989–9997.

[26] Y.T. Kim, Z. Jiao, N. Shikazono, J. Power Sources, 342 (2017) 787-795.

[27] Y. Nishida, S. Itoh, Electrochimica Acta, 56 (2011),2792-2800.
[28] B.S. Prakash, S.S. Kumar, S.T. Aruna, Renew. Sustain. Ener. Rev., 36 (2014)149-179.
[29] B. Kenney, M. Valdmanis, C. Baker, J.G. Pharoah, K. Karan, J. Power Sources, 189 (2009) 1051-1059.
[30] Y. Zhang, Y. Wang, Y. Wang, F. Chen, C. Xia, J. Power Sources, 196 (2011) 1983-1991.
[31] A. Bertei, H.-W. Choi, J.G. Pharoah, C. Nicolella, Powder Tech., 231 (2012) 44-53.
[32] K. Zheng, M. Ni, Sci. Bull., 61(1) (2016) 78–85.
[33] J. Golbert, C.S. Adjiman, N. Brandon, Ind. Eng. Chem. Res., 47 (2008) 7693-7699.
[34] C. Metcalfe, O. Kesler, T. Rivard, F. Gitzhofer, N. Abatzoglou, J. Electrochem. Soc., 157(9) (2010) B1326-B1335.
[35] Q. Cai, C.S. Adjiman, N. Brandon, Electrochimica Acta, 56 (2011) 5804-5814.
[36] K. Rhazaoui, Q. Cai, P. Shearing, C.S. Adjiman, N.P. Brandon, ECS Transactions, 35(1) (2011) 1097-1105.
[37] A. Ali, X. Wen, K. Nandakumar, J. Luo, K.T. Chuang, J. Power Sources, 185 (2008) 961-966.
[38] J. Sanyal, G.M. Goldin, H. Zhu, R.J. Kee, J. Power Sources, 195 (2010) 6671-6679.
[39] C. Lantuéjoul, Geostatistical Simulation, Model and Algorithms, Springer, 2002.
[40] Y. Suzue, N. Shikazono, N. Kasagi, J. Power Sources, 184 (2008) 52-59.
[41] M. Baniassadi, H. Garmestani, D.S. Li, S. Ahzi, M. Khaleel, X. Sun, Acta Mater., 59 (2011) 30-43.
[42] M. Neumann, J. Staněk, O.M. Pecho, L. Holzer, V. Beneš, V. Schmidt, Comput. Mater. Sci., 118 (2016) 353-364.
[43] A. Lanzini, P. Leone, P. Asinari, J. Power Sources, 194 (2009) 408–422.
[44] B. Abdallah, F. Willot, D. Jeulin, J. Microscopy, 263(1) (2016) 51-63.
[45] H.-W. Choi, D. Gawel, A. Berson, J.G. Pharoah, K. Karan, ECS Trans., 35(1) (2011) 997-1005.
[46] A. Galli, H. Beucher, G. Le Loc'h, B. Doligez, In "Geostatistical simulations", Ed. by M. Armstrong and P.A. Dowd, Quantitative Geology and Geostatistics: vol. 7, Springer Science+Business Media Dordrecht, 1994, 217-233.
[47] M. Armstrong, A. Galli, H. Beucher, G. Le Loc'h, D. Renard, B. Doligez, R. Eschard, F. Geffroy, Plurigaussian Simulations in Geosciences, Springer Heidelberg Dordrecht London New York, 2011
[48] P. Abrahamsen, A review of Gaussian random fields and correlation functions, Research Council of Norway, 1997.
[49] R.J. Adler, The geometry of random fields, Classics in applied mathematics, Siam, 2010.
[50] G. Delette, J. Laurencin, F. Usseglio-Viretta, J. Villanova, P. Bleuet, E. Lay, T. Le Bihan, Inter. J. Hydrogen Energy, 38 (2013) 12379-12391.
[51] J. Serra, Image analysis and mathematical morphology: Theoretical advances, Academic Press, Cornell University, 1988.
[52] P.M. Alder, C.G. Jacquin, J.A. Quiblier, Int. J. Multiphase Flow, 16 (July-August (4)) (1990) 691-712.
[53] Z.R. Liang, C.P. Fernandes, F.S Magnani, P.C. Philippi, J. Petrol. Sci. Eng. 21 (1998) 273-283.
[54] A. Lang, J. Potthoff, Monte Carlo Methods Appl., 17 (2011) 195-214.
[55] R.J. Wilson, D.J. Nott, Image Anal. Stereol., 20 (2001) 71-78.
[56] L. Bernadet, G. Gousseau, A. Chatroux, J. Laurencin, F. Mauvy, M. Reytier, Int. J. of Hydrogen Energy, 40 (2015) 12918-12928.

[57] M. Hubert, Durability of Solid Oxide Cells: an experimental and modelling investigation based on synchrotron X-ray nano-tomography characterization, Thesis of Grenoble University, 2017.
[58] M. Hubert, A. Pacureanu, C. Guilloud, Y. Yang, J.C. da Silva, J. Laurencin, F. Lefebvre-Joud, P. Cloetens, Submitted in: Applied Physics Letters (2017).
[59] E. Lay-Grindler, J. Laurencin, J. Villanova, I. Kieffer, F. Usseglio-Viretta, T. Le Bihan, P. Bleuet, A. Mansuy, G. Delette, ECS Trans. 57(1) (2013) 3177-3187.
[60] F. Usseglio-Viretta, J. Laurencin, G. Delette, J. Villanova, P. Cloetens, J. Power Sources, 256 (2014) 394-403.
[61] S.K. Bathia, J. Catalysis, 93 (1985) 192-196
[62] N. Epstein, Chem. Eng. Sci., 44(3) (1989) 77-779.
[63] D. Gostovic, J.R. Smith, D.P. Kundinger, K.S. Jones, E.D. Wachsmann, Electrochem. Solid State Letters, 10(12) (2007) B214-B217.
[64] J.R. Smith, A. Chen, D. Gostovic, D. Hickey, D. Kundinger, K.L. Duncan, R.T. DeHoff, K.S. Jones, E.D. Wachsman, Solid State Ionics, 180 (2009) 90–98.
[65] S.J. Cooper, D.S. Eastwood, J. Gelb, G. Damblanc, D.J.L. Brett, R.S. Bradley, P.J. Withers, P.D. Lee, A.J. Marquis, N.P. Brandon, P.R. Shearing, J. Power Sources, 247 (2014) 1033-1039.
[66] L. Holzer, D. Wiedenmann, B. Münch, L. Keller, M. Prestat, Ph. Gasser, I. Robertson, B. Grobéty, J. Mater. Sci., 48 (2013) 2934-2952.
[67] G. Gaiselmann, M. Neumann, V. Schmidt, O. Pecho, T. Hocker, L. Holzer, AIChE Journal, 60(6) (2014) 1983-1999.
[68] W. M. Harris, W. K. S. Chiu, Journal of Power Sources 282 (2015) 552-561.
[69] W. M. Harris, W. K. S. Chiu, Journal of Power Sources 282 (2015) 622-629.
[70] J. Laurencin, M. Hubert, K. Couturier, T. Le Bihan, P. Cloetens, F. Lefebvre-Joud, E. Siebert, Electrochimica Acta, 174 (2015) 1299-1316.
[71] H. Moussaoui, J. Debayle, Y. Gavet, J. Laurencin, Proc. SPIE – Int. Soc. Optical Eng. , Vol. 10338 (2017) doi:10.1117/12.2264376.
[72] John T.S. Irvine, D. Neagu, M.C. Verbraeken, C. Chatzichristodoulou, C. Graves, M.B. Mogensen, Nature Energy, 1 (2016) 1-13.
[73] F. Bidrawn, R. Küngas, J.M. Vohs, R.J. Gorte, J. Electrochem. Soc., 158(5) (2011) B514-B525.
[74] M. Naebe, K. Shirvanimoghaddam, Applied Materials Today, 5 (2016) 223-245.
[75] J. Kong, K. Sun, D. Zhou, N. Zhang, J. Mu, J. Qiao, J. Power Sources, 166 (2007) 337-342.
[76] L. Nie, Q. Sun, Z. Liu, M. Liu, Inter. J. Hydrogen Energy, 40 (2015) 16503-16508.
[77] J. Deseure, L. Dessemond, Y. Bultel, E. Siebert, J. Euro. Ceram. Soc., 25 (2005) 26-73-2676.
[78] L.C.R. Schneider, C.L. Martin, Y. Bultel, L. Dessemond, D. Bouvard, Electrochimica Acta, 52 (2007) 3190-3198.
[79] G. Anandakumar, N. Li, A. Verma, P. Singh, J.-H. Kim, J. Power Sources, 195 (2010) 6659-6670.
[80] D. Marinha, L. Dessemond, J. Scott Cronin, James R. Wilson, E. Djurado, Chem. Mater., *23* (24) (2011) 5340–5348.

[81] H. Moussaoui, R. Sharma, J. Laurencin, G. Delette, Y. Gavet, M. Hubert, P. Cloetens, J. Debayle, To be published in J. Power Sources (2018).
[82] John C Russ, Robert T. Dehoff, Practical Stereology, 2nd Edition, Springer 2001, pp. 35-39.
[83] P. Jouannot-Chesney, J.-P. Jernot, C. Lantuéjoul, Image analysis & stereology, 36(2) (2017) 95-103.

Appendix

1. Expression of the correlation $\rho_X(h)$ as a function of the weight function $\omega(h)$:

By definition, the correlation function $\rho_X(h)$ is the covariance of the random field $G_X(z)$:

$$\rho_X(h) = \mathrm{cov}\{G_X(z), G_X(z+h)\} \tag{A1}$$

Since G_X is defined as the convolution of an uncorrelated Gaussian random noise $U(z)$ with the weight function $\omega(h)$ (cf. eq. (7)), $\rho_X(h)$ can be expressed as follows:

$$\rho_X(h) = \mathrm{cov}\left\{ \sum_{h_1 \in \Omega} U(z-h_1)\omega(h_1), \sum_{h_2 \in \Omega} U(z+h-h_2)\omega(h_2) \right\} \tag{A2}$$

Considering the basic linear property of the covariance, the previous equation can be re-written as follows:

$$\rho_X(h) = \sum_{h_1 \in \Omega} \sum_{h_2 \in \Omega} \omega(h_1)\omega(h_2)\,\mathrm{cov}\{U(z-h_1), U(z+h-h_2)\} \tag{A3}$$

The covariance of the random noise is equal to 1 if $h_1 = h_2 - h$ and 0 otherwise. Besides, considering the symmetry of the weight function ($\omega(h) = \omega(-h)$), Eq. (A4) becomes:

$$\rho_X(h) = \sum_{h_2 \in \Omega} \omega(h_2 - h)\omega(h_2) = (\omega * \omega)(h) \tag{A4}$$

2. Relation between $C_X(h)$, $\rho_X(h)$ and λ_X:

The covariance $C_X(h)$ is defined as follows:

$$C_X(h) = P(z \in X, z+h \in X) = \int_{\lambda_X}^{+\infty} \int_{\lambda_X}^{+\infty} p(x_1, x_2)\,dx_1 dx_2 \tag{A5}$$

Where $p(x_1, x_2)$ is the bivariate distribution or probability density function given by:

$$p(x_1, x_2) = \frac{1}{2\pi\sqrt{1-\rho^2}} \exp\left\{ \frac{-\left(x_1^2 + x_2^2 + 2\rho x_1 x_2\right)}{2\left(1-\rho^2\right)} \right\} \tag{A6}$$

It can be easily demonstrated that $\dfrac{\partial p}{\partial \rho} = \dfrac{\partial^2 p}{\partial x_1 \partial x_2}$ and then:

$$\frac{\partial C_X(h)}{\partial \rho} = \int_{\lambda_X}^{+\infty} \int_{\lambda_X}^{+\infty} \frac{\partial^2 p(x_1, x_2)}{\partial x_1 \partial x_2} dx_1 dx_2 = p(\lambda_X, \lambda_X) \tag{A7}$$

The integration of the previous equation, $\int_{r=1}^{r=\rho} \dfrac{\partial C_X(h)}{\partial \rho} dr = \int_{r=1}^{r=\rho} p(\lambda_X, \lambda_X) dr$, leads to the relation used in the method:

$$C_X(h) - \varepsilon_X = \frac{1}{2\pi} \int_1^{\rho_X(h)} \frac{1}{\sqrt{1-r^2}} \exp\left\{ \frac{-\lambda_X^2}{1+r} \right\} dr \tag{A8}$$

List of Symbols

$i = X, Y, Z$	Phase name	(–)
$\bar{i}$	Complementary phase of i	(–)
C_i	The covariance function of i	(–)
ε_i	The volume fraction of i	(–)
S_p^i	The specific surface area of i	(μm^{-1})
$S_p^{i,j}$	The interfacial specific surface area between i and j	(μm^{-1})
Ω	3D domain	(–)
V_Ω	Domain volume	(μm^3)
G_i	Random Gaussian field of phase i	(–)
λ_X	Threshold	(–)
$N(0,1)$	Standard Normal Distribution	(–)
U	Uncorrelated Gaussian random noise	(–)
ω	The weight function	(–)
ρ_i	The correlation function of i	(–)
p	Probability density function	(–)
FFT	Fast Fourier Transform	(–)
l	Correlation length	(µm)
G_{ij}	Bi-Gaussian random field	(–)
D_i	Domain or Cell related to the phase i	(–)
π	Mathematical constant Pi ≈ 3.1416	(–)
ξ_{TPB}	Density of Triple Phase Boundaries lengths	(μm^{-2})
τ_i^{geo}	Geometrical tortuosity	(–)
β_i	Constrictivity parameter	(–)
M_i	Microstructure-factor	(–)
d_p	Mean phase diameter	(µm)
δ	Proportion of connected phase	(–)